Growth of antiperovskite oxide Ca3SnO films by pulsed laser deposition

doi: 10.1016/j.jcrysgro.2018.08.014

Growth of Antiperovskite Oxide Ca_3SnO Films by Pulsed Laser Deposition

Makoto Minohara[1,2]*, Ryu Yukawa[1], Miho Kitamura[1], Reiji Kumai[1,2], Youichi Murakami[1,2] and Hiroshi Kumigashira[1,2]

*Corresponding author Tel: +81 29 864 5586

E-mail: minohara@post.kek.jp

[1]*Photon Factory, Institute of Materials Structure Science (IMSS), High Energy Accelerator Research Organization (KEK), Tsukuba, Ibaraki 305-0801, Japan*

[2]*Department of Materials Structure Science, SOKENDAI (The Graduate University for Advanced Studies), Tsukuba, Ibaraki 305-0801, Japan*

Abstract

We report the epitaxial growth of Ca_3SnO antiperovskite oxide films on (001)-oriented cubic yttria-stabilized zirconia (YSZ) substrates by using a conventional pulsed laser deposition (PLD) technique. In this work, a sintered Ca_3SnO pellet is used as the ablation target. X-ray diffraction measurements demonstrate the (001) growth of Ca_3SnO films with the antiperovskite structure and a cube-on-cube orientation relationship to the YSZ substrate. The successful synthesis of the antiperovskite phase is further confirmed

by x-ray photoemission spectroscopy. These results strongly suggest that antiperovskite-oxide films can be directly grown on substrates from the target material using a PLD technique.

Keywords

A3. Pulsed laser deposition

B1. Antiperovskite oxides

B1. Stannate

A1. Oxide electronics

Main text

1. Introduction

Perovskite oxides are an important class of materials that exhibit novel functional properties [1]. Recently, their counterpart materials, namely antiperovskite oxides A_3BO (A = Ca, Sr, Ba; B = Sn, Pb), have been attracting attention as an alternative platform for prospecting unique physical properties. Following the theoretical prediction that some materials in the antiperovskite-oxide family have three-dimensional Dirac fermions [2], a number of experimental and theoretical efforts have been devoted to exploring the possible presence of bulk Dirac fermions in antiperovskite oxides [3-9]. Since this unique electronic structure is predicted to appear in the bulk and not at the surface, heterostructures composed of perovskite and antiperovskite oxides might also be promising candidates for exploratory studies of novel physical properties, analogous to the studies of perovskite oxide

heterostructures [10-14]. Despite these intriguing research opportunities, there are few reports on the growth of antiperovskite-oxide films [7,8], although there are a lot of works on the growth of antiperovskite-nitride films [15-19]. Since the pulsed laser deposition (PLD) technique is capable of growing films from a wide variety of materials, this technique is well-suited for the rapid investigation of antiperovskite-oxide films. However, since the use of PLD for the growth of these films is still in its infancy, whether antiperovskite-oxide films can be really grown by PLD remains to be convincingly answered. X-ray diffraction (XRD) measurements from the reported antiperovskite-oxide films grown by an "unconventional" PLD technique, where the films were grown by alternating deposition of AO and BO_2 targets, did not show any of the characteristic Bragg reflections from (00l) planes with an odd l that should be expected for an antiperovskite phase [7]. Therefore, the development of reliable methods for the growth of antiperovskite-oxide films by PLD is necessary, not only for exploring novel functionalities, but also for elucidating unique band structures via spectroscopic measurements [20-22].

In this study, we report the conventional PLD growth of an antiperovskite-oxide Ca_3SnO film by using the antiperovskite-oxide ceramic target as the source material. By varying the substrate temperature ($T_{sub.}$) and the oxygen partial pressure (P_{O2}) during growth, we identify the optimum growth condition for Ca_3SnO thin films. XRD results indicate the formation of the antiperovskite structure and its cube-on-cube epitaxial relationship to the substrate. The successful growth of antiperovskite phase is further confirmed by x-ray photoemission spectroscopy (XPS): The shape of the valence band spectrum is qualitatively reproduced by the first-principles calculation for Ca_3SnO.

2. Experimental Section

Ca_3SnO films were grown on (001)-oriented yttria-stabilized zirconia (YSZ) single-crystal substrates in a vacuum chamber by a PLD technique using a sintered Ca_3SnO target. A Nd-doped yttrium aluminum garnet laser was used for ablation in its frequency-tripled mode (λ = 355 nm) at a repetition rate of 1 Hz. Prior to film deposition, YSZ substrates were annealed in air, in an electric furnace at 1400 ºC, to obtain an atomically flat surface. To optimize the growth conditions, $T_{sub.}$ and P_{O2} were varied under a fixed laser fluence of ~4.6 mJ/cm^2. Typical thickness (growth rate) of the films was estimated to be about 13 nm (~0.004 nm/sec) estimated from the Laue fringes of (002) Brag peaks (see the Supplementary Material). The surface crystalline quality during growth was monitored *in situ* by reflective high-energy electron diffraction (RHEED).

The epitaxial relationship and crystalline quality were analyzed using *ex situ* synchrotron-based XRD, which was carried out at beamline 7C in the Photon Factory, KEK. The energy of the incident x-ray was 9 keV. As previously mentioned, (001) and/or (003) Bragg peaks are key to distinguishing the formation of antiperovskite structure. However, the intensity of these peaks is relatively much weaker than (00*l*) peaks with an even *l*. Therefore, the use of synchrotron-based XRD measurement with high sensitivity and resolution is necessary in the present study. For XRD measurements, an Au film with a thickness of ~24 nm was evaporated as a capping layer to prevent degradation by moisture in the air as following: The grown films were transported to an evaporation chamber using the home-built vacuum suitcase where the samples were kept under the vacuum of less than 10^{-6} Torr, and the Au film was deposited by a conventional resistive heating evaporator. As discussed later in detail, the unintentional sample heating and outgassing during the Au evaporation may cause the formation of some interfacial reaction layers between Au and

Ca_3SnO owing to the high chemical activity of Ca_3SnO [23].

XPS measurements were performed using a VG-Scienta R3000 electron energy analyzer with a monochromatized Al $K\alpha$ x-ray source ($h\nu$ = 1486.6 eV). For XPS measurements, the samples were transported to an analysis chamber without air exposure using the home-built vacuum suitcase just after Ca_3SnO film growth and measured under the vacuum of 10^{-10} Torr as soon as possible in order to minimize unavoidable surface reactions even under the ultrahigh vacuum. Binding energies were calibrated by measuring a gold film, electrically connected to the samples. All spectra were acquired at room temperature with a total energy resolution of 500 meV.

First-principles calculations based on density-functional theory were carried out in the framework of the Perdew-Burke-Ernzerhof-type generalized-gradient approximation [24] using the WIEN2k code [25], where spin-orbit interactions are taken into account. An idealized cubic structure was assumed with the empirical lattice constant of a = 4.83 Å [23]. The corresponding Brillouin zone was sampled by 20 × 20 × 20 momentum points.

3. Results and discussion

3.1 Optimization of the growth conditions for Ca_3SnO films

In general, the guidance of Ellingham diagrams, in which the stable valence states of simple metal oxides are mapped in terms of standard-state Gibbs free energy and temperature, is useful in deducing optimal growth conditions. However, since Ca_3SnO exhibits an unusual Sn valence state of Sn^{4-}, it is difficult to identify the processing "sweet spot" using the Ellingham diagram, as there are no thermodynamic data available for Sn^{4-} [26,27]. Therefore, we optimize Ca_3SnO thin film growth by varying $T_{sub.}$ and P_{O2} over a

rather wide range of values. Figure 1(a) shows the RHEED patterns for the thin films grown at various $T_{sub.}$ and P_{O2}. There are two discrete regions showing the clear streak patterns indicative of the epitaxial growth of certain oxides; A region at $T_{sub.}$ = 900 ºC without oxygen flow and another between $T_{sub.}$ = 700 and 750 ºC under a P_{O2} of 10^{-6} to 10^{-7} Torr. Since the RHEED pattern changes in a discontinuous manner, we surmise that different oxides are grown under these two discrete conditions. In order to survey the chemical composition of these thin films, we performed auger electron spectroscopy (AES). Figure 1(b) shows AES results for samples α ($T_{sub.}$ = 900 ºC, without oxygen flow) and β ($T_{sub.}$ = 700 ºC, P_{O2} = 10^{-7} Torr), representative of the above-mentioned regions [also see Fig. 1(a)]. The AES results reveal the difference between these samples. While sample α does not contain Sn ions, sample β does. The disappearance of Sn for the sample α may originate from the high volatility of Sn and its oxides (SnO and SnO_2) [28] at $T_{sub.}$ = 900 ºC, strongly suggesting that only the growth of the remnant CaO_x is stabilized at this higher temperature region. Indeed, in the XRD pattern for the sample grown in the almost same conditions to sample α exhibited the only CaO (111) peak (see the Supplemental Material). From these results, the optimum conditions for Ca_3SnO growth could be in the range of $T_{sub.}$ = 700 to 750 ºC under a P_{O2} of 10^{-6} to 10^{-7} Torr.

3.2 Structural analysis

We performed XRD measurements to verify the formation of antiperovskite Ca_3SnO. Figure 2(a) shows the out-of-plane XRD 2θ-θ pattern for the sample β. Some characteristic peaks are clearly observed. In order to index these peaks, we compare the measured 2θ-θ XRD pattern with the calculated patterns of Ca_3SnO (antiperovskite

structure), $CaSnO_3$ (perovskite structure), and CaO (rocksalt structure), since $CaSnO_3$ and CaO are also potentially synthesized under such an oxidizing atmosphere [26-28]. The calculated (00*l*) and (*l l l*) Bragg peaks of the three potential oxides are shown in the Fig. 2(b). Comparison of the measured XRD pattern with the calculated patterns shows that the observed peaks in Fig. 2(a) correspond to the characteristic (00*l*) Bragg peaks of Ca_3SnO. Since rocksalt CaO and Ca_3SnO have near identical lattice constants, a (00*l*) peak with an odd *l* is key to distinguishing these two structures. Since a (001) peak is observed, the XRD results provide strong evidence for the formation of antiperovskite Ca_3SnO films by PLD under the identified optimum conditions, although the existence of some "impurity" phases is surveyed. Considering both the formation energy in the materials project database [29] and the calculated peak positions of candidate materials comprised of Ca, Sn and O atoms [29], the possible impurities might be CaO, $Ca_2Sn_3O_8$ or Ca_2SnO_4.

From the observed (00*l*) Bragg peaks of the Ca_3SnO film, the lattice constant is determined to be 0.481 ± 0.001 nm. The value was further confirmed by the reciprocal space mapping (Fig. S2 in the Supplementary Material), where the almost identical in-plane and out-of-plane lattice constant (0.481 ± 0.001 and 0.480 ± 0.001 nm, respectively) were obtained. The results indicate that the Ca_3SnO film is fully relaxed owing to the significant lattice mismatch of 7.1 % between Ca_3SnO (0.483 nm) [23] and YSZ (0.516 nm) [30]. The slight deviation from the bulk value of 0.483 nm suggests the existence of some structural disorders. Indeed, the intensity ratio of (001) to (002) Bragg peaks is evaluated to be 0.18, which is slightly smaller than the ideal ratio of 0.27, supporting the presence of structural disorder in the Ca_3SnO films owing to the formation of impurity phases and a possible off-stoichiometry composition [8].

Here, we discuss the possible origin of "impurity" peak observed in Fig. 2(a).

The successful achievement of the epitaxial Ca_3SnO film has been confirmed by the observation of clear Laue fringe around a Ca_3SnO (002) Bragg reflection (Fig. S1 in the Supplementary Material), as well as the good agreement of XRD pattern with the simulated one [Figs. 2(a) and (b)]. This strongly suggests that the "impurity phase" in XRD profile may originate not from impurity phases in Ca_3SnO films but from some interfacial reaction layers formed between Au and Ca_3SnO owing to the high chemical activity of Ca_3SnO: some chemical reaction may occur in the interface region of Ca_3SnO during Au deposition process as well as the XRD measurements in air. In fact, the intensity corresponding the "impurity phases" significantly depended on samples of Au/Ca_3SnO, which might originate from the difference in unintentional Au-deposition conditions and in time from sample fabrication to XRD measurements (see Supplemental Material). Based on these experimental results, it is naturally concluded that such an interfacial reaction layer is the origin of "impurity phases" in the XRD profile. In fact, the XRD pattern obtained with special sample treatments did show negligible impurity signal [Fig. S3(c) in the Supplementary Material]. It should be noted that the peak position of "impurity phases" show close agreement with that of CaO (111) and/or Ca_3SnO (111), implying the preferential formation of (111) plane even on (001)-plane films [16]. Since the precise identification of the "impurity" peak is difficult at the moment, further systematic investigation is necessary to clarify its origin.

Next, we investigate the crystalline quality of Ca_3SnO films and its epitaxial relationship with YSZ (001) substrate. As shown in Fig. 2(c), the full-width at half-maximum of the rocking curve for the (002) diffraction is evaluated to be around 0.14º. This value is one order of magnitude narrower than that of Sr_3PbO antiperovskite films grown by molecular beam epitaxy [8]. This result identifies the current PLD-grown films as being highly crystalline, despite the impurity phases observed in the 2θ-θ pattern. Figure

2(d) shows the *phi*-scan of XRD patterns on {202} reflections for Ca_3SnO films, together with that of YSZ substrates with cubic symmetry. The peaks are clearly observed every 90° for the film as well as the substrate, reflecting the four-fold symmetry of antiperovskite structure. This result indicates the cube-on-cube epitaxial relationship between the YSZ (001) substrate and the Ca_3SnO film despite the significant lattice mismatch of 7.1 % between Ca_3SnO and YSZ.

3.3 Chemical state analysis

In order to analyze the chemical state of constituent elements, XPS measurements were performed on the Ca_3SnO film (sample β). The XPS spectra for Sn-3*d*, Ca-2*p*, and O-1*s* core levels are shown in Figs. 3(a), (b), and (c), respectively, along with the results of peak deconvolution by curve-fitting analysis. Since the intensity of the peaks at higher binding energies became stronger with increasing photoelectron emission angle (see Fig S4 in the Supplemental Material), the higher (lower) peaks can be assigned to the surface (bulk) components for all core levels. For the Sn-3*d* core level, the bulk and surface components for Sn $3d_{5/2}$ states are evaluated to be positioned at energies of ~ 484.8 eV and ~486.7 eV, respectively. In terms of chemical shift, the surface component can be assigned to either Sn^{4+} (486.0–487.3 eV) or Sn^{2+} (485.6–487 eV) [31], suggesting the segregation of Sn oxides (SnO_2 or SnO, respectively) to the surface of the Ca_3SnO films.

On the other hand, the peak position of the bulk component is unusual in oxides: The energy of ~484.8 eV for Sn $3d_{5/2}$ states is close to that of Sn metal or its intermetallic alloys (Sn^0: 484.3–485.2 eV) [31]. The unusual chemical shift of Sn ions might imply the existence of possible Sn^{4-} states in Ca_3SnO as following reasons, although the chemical shift of Sn^{4-} is not known yet. Assuming that the Sn ions in Ca_3SnO are close to Sn^0 states

(antiperovskite Ca_3SnO is an intermetallic), the Ca ions should be also close to Ca^0. However, as shown in Fig. 3(b), the peak position of the bulk Ca $2p_{3/2}$ states (346.8 eV) is significantly different from that of Ca metal and its alloys (344.9-346.0 eV) [31]. Based on the chemical shifts of Ca^{2+} states (346.1–347.3 eV) [31], the valence of Ca ions in the Ca_3SnO film is assigned to Ca^{2+}. Moreover, the chemical shift of the O-1*s* core level can be also ascribed to O^{2-} as shown in Fig. 3(c) [31]. From these experimental results, it could be reasoned that Sn ions in Ca_3SnO are close to an unusual valence state of Sn^{4-}, although further theoretical investigation is necessary to clarify such an unusual the chemical states of Sn ions in Ca_3SnO.

3.4 Analysis of electronic structure

The successful synthesis of the antiperovskite phase of Ca_3SnO is further supported by valence band (VB) spectra shown in Fig. 4. Here, we would like to emphasize again that the influence of "impurities" phase observed in the XRD measurements [Fig. 2(a)] on the XPS results is negligible, because the samples were transported to an analysis chamber under the ultrahigh vacuum just after film growth as mentioned in the experimental section. The upper panel of Fig. 4 shows the VB spectrum of Ca_3SnO film (sample β), together with the density of states (DOS) obtained by the first-principles calculations. The reported XPS spectra of CaO [32], $CaSnO_3$ [33], SnO_2 [34], SnO [34], and Sn metal [35] are shown in the lower panel of Fig. 4 as references. Overall, the VB spectrum of Ca_3SnO film is significantly different from those of the referenced materials, suggesting that the formation of Ca_3SnO is distinguished by the XPS spectra even if other materials exist as impurity phases. The characteristic feature in the Ca_3SnO spectrum is the existence of a band in the energy range between the Fermi level and ~3 eV. This feature of the VB spectra is

approximately captured by the first-principles calculation for Ca_3SnO, although there are some discrepancies in the peak positions for bands located at higher binding energies (upper panel, Fig. 4). Therefore, the XPS results provide additional confirmation of the formation of Ca_3SnO.

4. Conclusions

We have demonstrated that the antiperovskite oxide Ca_3SnO film can be grown on a YSZ (001) substrate by using a Ca_3SnO target in a conventional pulsed laser deposition (PLD) technique. By varying the temperature of the substrate and the partial pressure of oxygen during growth, we identified the optimal conditions for the PLD growth of Ca_3SnO films. The successful growth of epitaxial Ca_3SnO films on YSZ substrates is confirmed by x-ray diffraction measurements. The *phi*-scan of {202} reflections reveals the cube-on-cube epitaxial relationship between the Ca_3SnO film and the YSZ (001) substrate. The synthesis of the antiperovskite phase of Ca_3SnO is further supported by x-ray photoemission spectroscopy. The results show that antiperovskite-oxide films can be directly synthesized from the target by using a PLD technique just like several other widely-studied oxide films. The present demonstration of the growth of antiperovskite oxides by PLD might be a promising avenue for the research of antiperovskite oxides in film form as well as artificial antiperovskite/perovskite oxide structures.

Acknowledgments

We thank Hironori Nakao for useful discussions. This work was supported by a Grant-in-Aid for Scientific Research (No. B25287095 and 16H02115) and a Grant-in-Aid

for Young Scientists (No. 15K17470 and 18K04946) from the Japan Society for the Promotion of Science (JSPS) as well as the MEXT Elements Strategy Initiative to Form Core Research Center. The work at KEK-PF was performed under the approval of the Program Advisory Committee (Proposals No. 2013S2-002 and 2015S2-005) at the Institute of Materials Structure Science, KEK.

References

1) H. Y. Hwang, Y. Iwasa, M. Kawasaki, B. Keimer, N. Nagaosa, and Y. Tokura, Nat. Mater. **11**, 103 (2012).
2) T. Kariyado, and M. Ogata, J. Phys. Soc. Jpn. **80**, 083704 (2011).
3) M. Klintenberg, J. T. Haraldsen, and A. V. Balatsky, Appl. Phys. Res. **6**, 31 (2014).
4) T. H. Hsieh, J. Liu, and L. Fu, Phys. Rev. B **90**, 081112 (2014).
5) M. Oudah, A. Ikeda, J. N. Hausmann, S. Yonezawa, T. Fukumoto, S. Kobayashi, M. Sato, and Y. Maeno, Nat. Commun. **7**, 13617 (2016).
6) Y. Okamoto, A. Sakamaki, and K. Takenaka, J. Appl. Phys. **119**, 205106 (2016).
7) Y. F. Lee, F. Wu, R. Kumar, F. Hunte, J. Schwartz, and J. Narayan, Appl. Phys. Lett. **103**, 112101 (2013).
8) D. Samal, H. Nakamura, and H. Takagi, APL Mater. **4**, 076101 (2016).
9) Y. Obata, R. Yukawa, K. Horiba, H. Kumigashira, Y. Toda, S. Matsuishi, and H. Hosono, Phys. Rev. B **96**, 155109 (2017).
10) A. Ohtomo, and H. Y. Hwang, Nature **427**, 423 (2004).
11) N. Reyren, S. Thiel, A. D. Caviglia, L. F. Kourkoutis, G. Hammerl, C. Richter, C. W. Schneider, T. Kopp, A. S. Ruetschi, D. Jaccard, M. Gabay, D. A. Muller, J. M. Triscone, and J. Mannhart, Science **317**, 1196 (2007).
12) K. S. Takahashi, M. Kawasaki, and Y. Tokura, Appl. Phys. Lett. **79**, 1324 (2001).
13) T. Koida, M. Lippmaa, T. Fukumura, K. Itaka, Y. Matsumoto, M. Kawasaki, and H. Koinuma, Phys. Rev. B **66**, 144418 (2002).
14) S. J. May, A. B. Shah, S. G. E. te Velthuis, M. R. Fitzsimmons, J. M. Zuo, X. Zhai, J. N. Eckstein, S. D. Bader, and A. Bhattacharya, Phys. Rev. B **77**, 174409 (2008).
15) M. Magnuson. M. Mattesini, C. Höglund, I. A. Abrikosov, J. Birch, and L. Hultman, Phys.

Rev. B **78**, 235102 (2008).

16) Y. Na, C. Wang, Y. Sun, L. Chu, M. Nie, N. Ji, and J.-P. Wang, Mater. Res. Bull. **46**, 1022 (2011).

17) D. D. Vaughn II, J. Araujo, P. Meduri, J. F. Callejas, M. A. Hickner, and R. E. Schaak, Chem. Mater. **26**, 6226 (2014).

18) F. Yu, L. Ren, M. Meng, Y. Wang, M. Yang, S. Wu, and S. Li, J. Appl. Phys. **115**, 133911 (2014).

19) C. X. Quintela, N. Campbell, D. F. Shao, J. Irwin, D. T. Harris, L. Xie, T. J. Anderson, N. Reiser, X. Q. Pan, E. Y. Tsymbal, M. S. Rzchowski, and C. B. Eom, APL Mater **5**, 096103 (2017).

20) T. Ohta, A. Bistwick, J. L. McChesney, T. Seyller, K. Horn, and E. Rotenberg, Phys. Rev. Lett. **98**, 206802 (2007).

21) D. Hsieh, D. Qian, L. Wray, Y. Xia, Y. S. Hor, R. J. Cava, and M. Z. Hasan, Nature **452**, 970 (2008).

22) S.-Y. Xu, N. Alidoust, I. Belopolski, Z. Yuan, G. Bian, T.-R. Chang, H. Zheng, V. N. Strocov, D. S. Sanchez, G. Chang, C. Zhang, D. Mou, Y. Wu, L. Huand, C.-C. Lee, S.-M. Huang, B. K. Wang, A. Bansil, H.-T. Jeng, T. Neupert, A. Kaminski, H. Lin, S. Jia, and M. Z. Hasan, Nat. Phys. **11**, 748 (2015).

23) A. Widera and H. Schäfer, Mater. Res. Bull. **15**, 1805 (1980).

24) J. P. Perdew, K. Burke, and M. Ernzerhof, Phys. Rev. Lett. **77**, 3865 (1996).

25) P. Blaha, K. Schwarz, G. K. H. Madsen, D. Kvasnicka, and J. Luitz: *WIEN2k, An Augmented Plane Wave + Local Orbitals Program for Calculating Crystal Properties* (Karlheinz Schwarz, Techn. Universität Wien, Austria, 2001) ISBN 3-9501031-1-2.

26) *CRC Handbook of Chemistry and Physics*, 61st ed.; Weast, R. C., Astle, M. J., Eds.; CRC

Press: Boca Raton, FL, 1980; pp D67-77.

27) *NIST Chemistry WebBook, NIST Standard Reference Database Number 69*, edited by P. J. Linstrom and W. G. Mallard. http://webbook.nist.gov/chemistry/.

28) I. Barin, O. Knacke, and O. Kubaschewski, In Thermochemical Properties of Inorganic Substances (Springer, 1977).

29) A. Jain, S. P. Ong, G. Hautier, W. Chen, W. D. Richards, S. Dacek, S. Cholia, D. Gunter, D. Skinner, G. Ceder, and K. A. Persson, APL Mater. **1**, 011002 (2013).

30) I. R. Gibson, and T. S. Irvine, J. Mater. Chem. **6**, 896 (1996).

31) *NIST X-ray Photoelectron Spectroscopy Database, NIST Standard Reference Database Number 20*, edited by A. V. Naumkin, A. Kraut-Vass, S. W. Gaarenstroom, and C. J. Powell. https://srdata.nist.gov/xps/.

32) D. Ochs, B. Braun, W. Maus-Friedrichs, and V. Kempter, Surf. Sci. **417**, 406 (1998).

33) J. D. Baniecki, T. Yamazaki, D. Ricinschi, Q. V. Overmeere, H. Aso, Y. Miyata, H. Yamada, N. Fujimura, R. Maran, T. Anazawa, N. Valanoor, and Y. Imanaka, Sci. Rep. **7**, 41725 (2017).

34) Y. Ogo, H. Hiramatsu, K. Nomura, H. Yanagi, T. Kamiya, M. Kimura, M. Hirano, and H. Hosono, Phys. Status Solidi A **206**, 2187 (2009).

35) H. Höchst, S. Hüfner, and A. Goldman, Solid State Commun. **19**, 899 (1976).

Figure Captions

Fig. 1 (Color online) (a) A map of RHEED patterns from thin films grown on a YSZ (001) substrate at various $T_{sub.}$ and P_{O2}. (b) Auger electron spectra of thin films labeled α and β that are grown at $T_{sub.}$ = 900 ºC with no oxygen flow (red) and $T_{sub.}$ = 700 ºC with $P_{O2} = 10^{-7}$ Torr (blue), respectively.

Fig. 2 (Color online) (a) The 2θ-θ XRD pattern of sample β. The asterisks indicate the peaks from a capped gold film, which are indexed as (111), (002), and (222) Bragg reflections from left side, while the diamonds are from "impurities". (b) Calculated XRD patterns for Ca_3SnO, $CaSnO_3$, and CaO. The black and gray bars correspond to (00*l*) and (*l l l*) peaks, respectively. (c) The rocking curve for the (002) Bragg reflection of grown films. (d) *phi*-scans for {202} reflection of the YSZ substrate (upper panel) and grown thin film (lower panel).

Fig. 3 (Color online) XPS spectra from the Ca_3SnO film (sample β) for (a) Sn-3*d*, (b) Ca-2*p*, and (c) O-1*s* core levels. The fitting results are overlaid by green, blue, and red curves, which correspond to the surface component (*S*), bulk component (*B*), and their summation, respectively.

Fig. 4 (Color online) (upper panel) The valence band spectrum of a Ca_3SnO film (sample β), together with the DOS obtained from the first principle calculation. In order to emphasize the gap-like feature in the Ca_3SnO film near the Fermi level (E_F) of the sample, the Fermi edge of gold film is superimposed. (Lower panel) The reference spectra of CaO [32], $CaSnO_3$ [33], SnO_2 [34], SnO [34], and Sn metal [35].

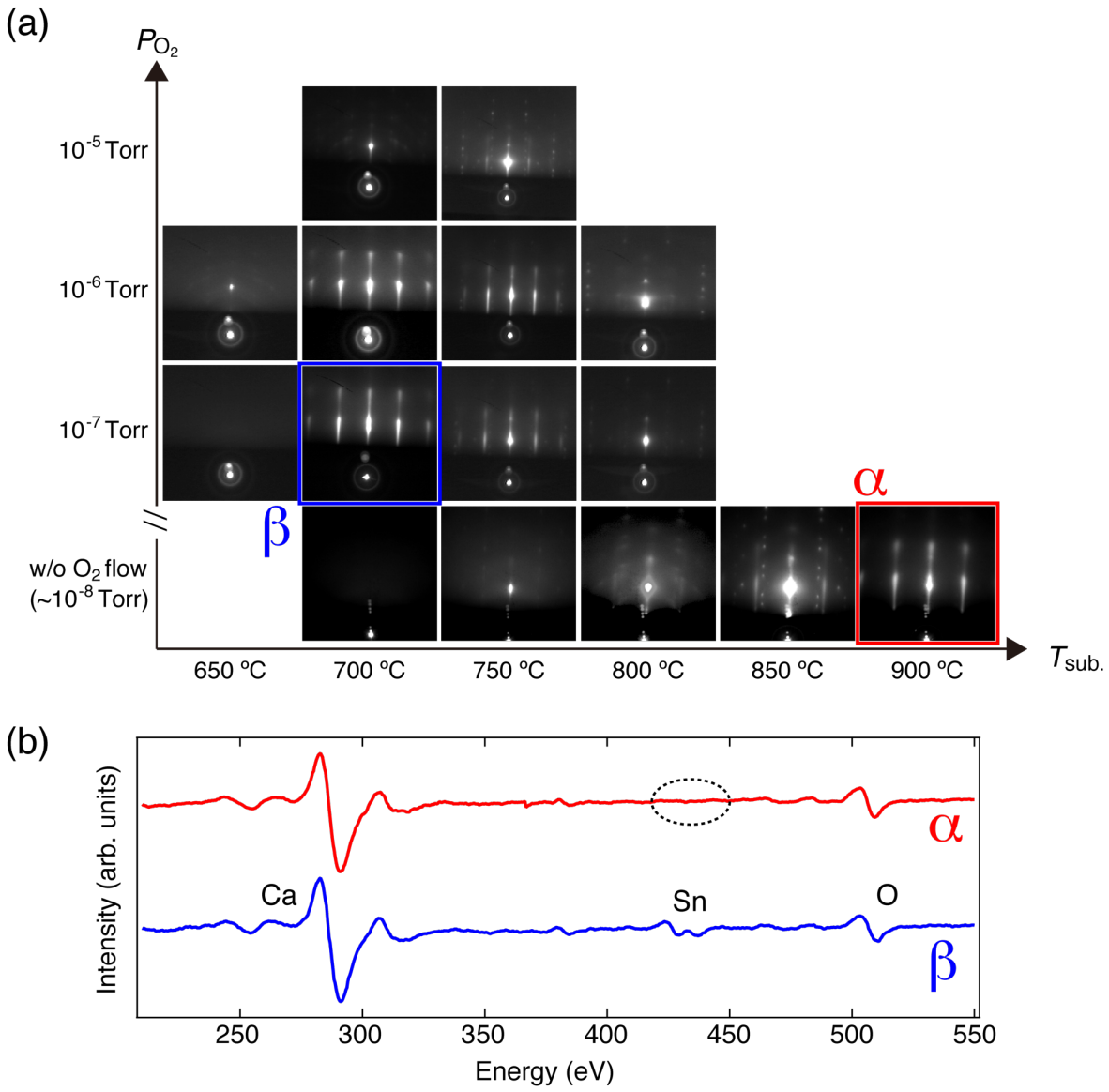

Fig. 1. (Color Online)

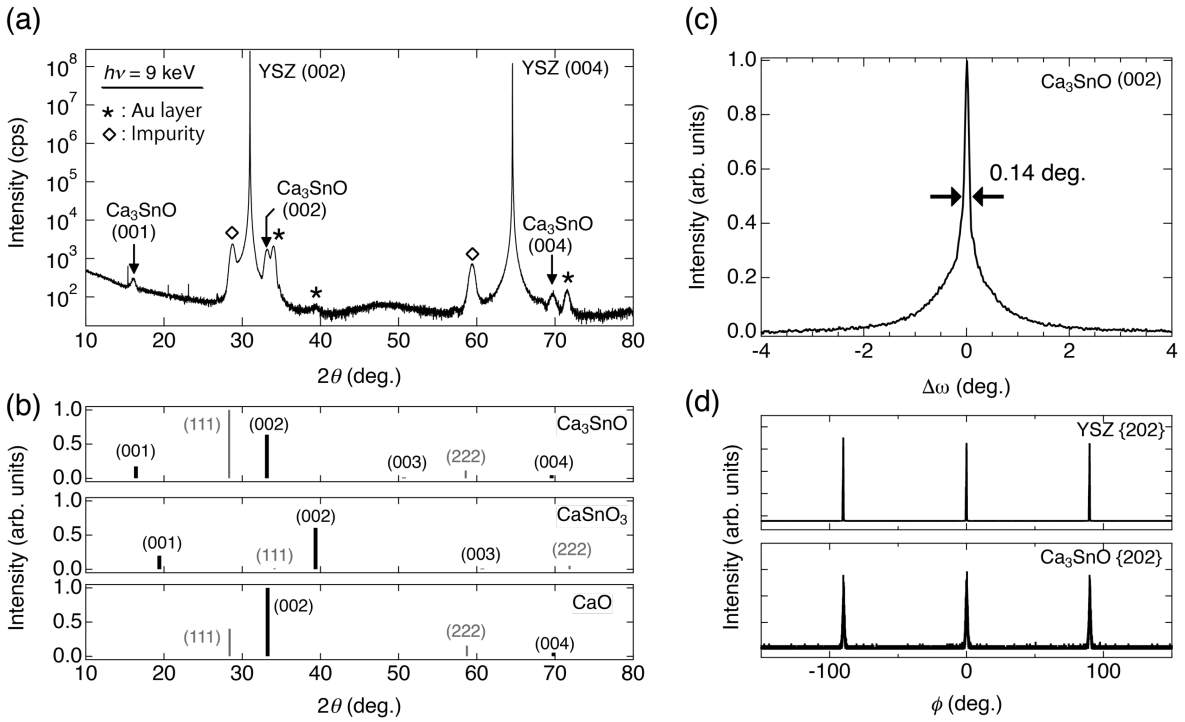

Fig. 2. (Color Online)

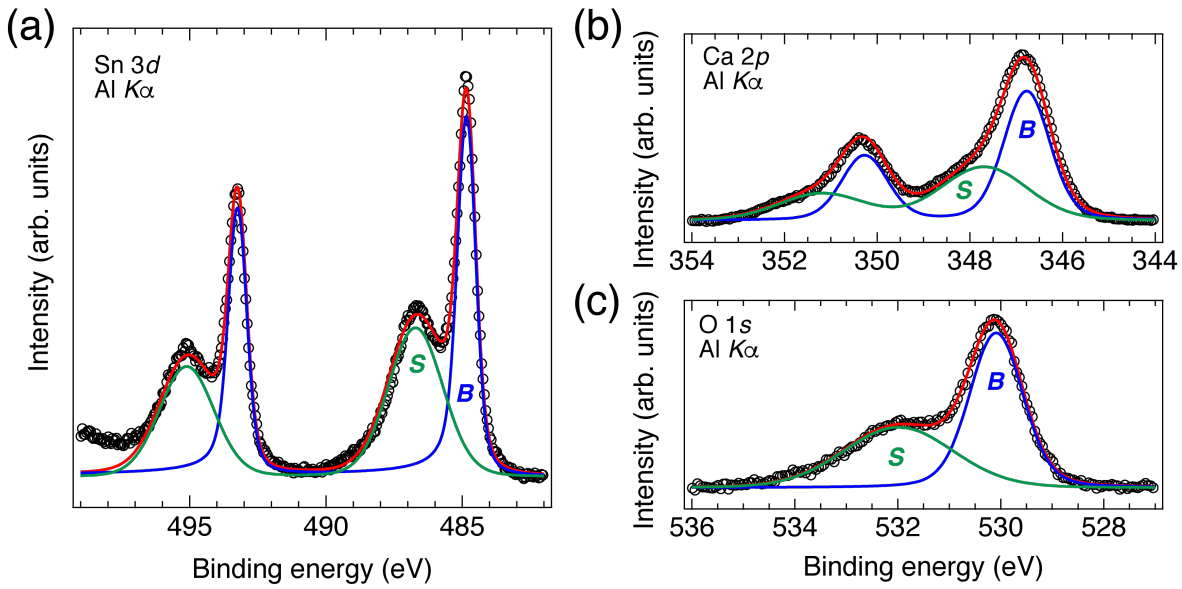

Fig. 3. (Color Online)

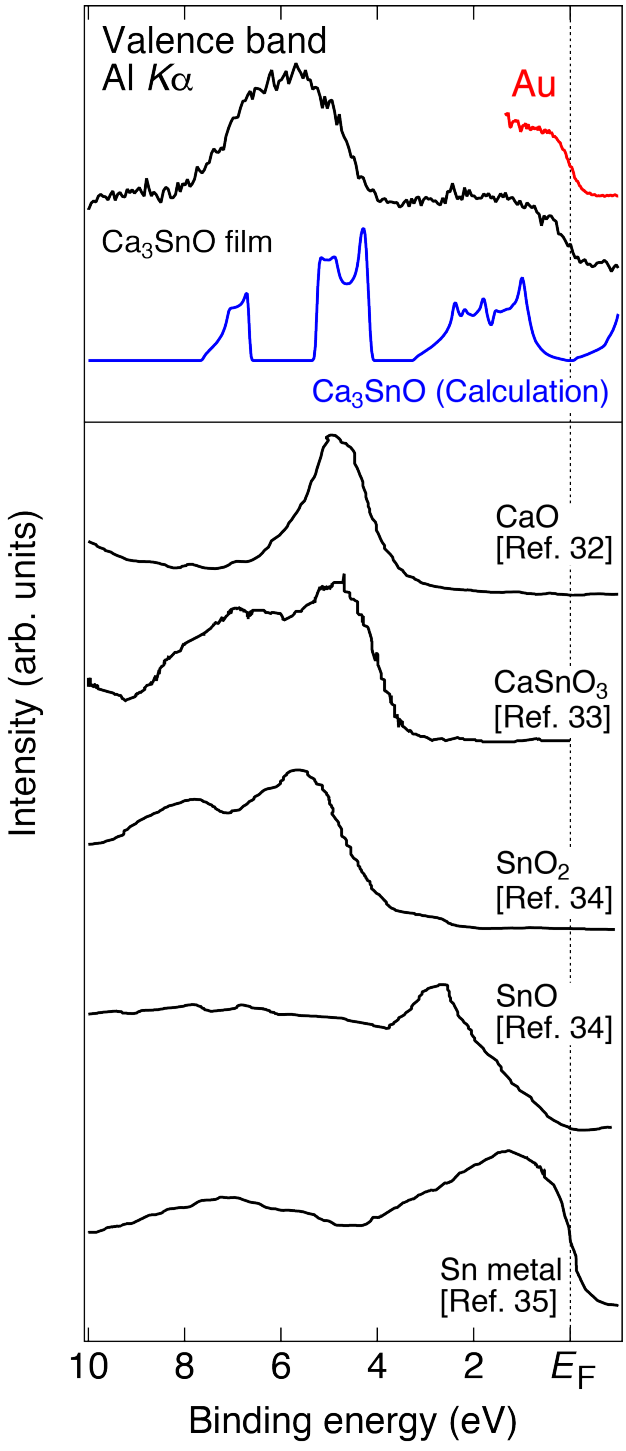

Fig. 4. (Color Online)

Supplemental Material: Growth of Antiperovskite Oxide Ca_3SnO Films by Pulsed Laser Deposition

Makoto Minohara[1,2]*, Ryu Yukawa[1], Miho Kitamura[1], Reiji Kumai[1,2], Youichi Murakami[1,2] and Hiroshi Kumigashira[1,2]

[1]*Photon Factory, Institute of Materials Structure Science (IMSS), High Energy Accelerator Research Organization (KEK), Tsukuba, Ibaraki 305-0801, Japan*

[2]*Department of Materials Structure Science, SOKENDAI (The Graduate University for Advanced Studies), Tsukuba, Ibaraki 305-0801, Japan*

*Author to whom correspondence should be addressed; minohara@post.kek.jp

This PDF file includes:

Fig. S1, S2, S3, and S4

Estimation of the thickness of Ca_3SnO film

Owing to the high chemical activity of Ca_3SnO [S1], it is difficult to determine the film thickness by any conventional methods such as a contact-type thickness meter or x-ray reflectivity. Therefore, we have alternatively estimated the film thickness by using the Laue fringes around (002) Bragg reflection of Ca_3SnO layer of Au/Ca_3SnO. Figure S1 shows synchrotron-based x-ray diffraction patterns which are magnified around (002) diffraction. A red line is identical to the 2θ-θ XRD patterns shown Fig. 1(a), which has been measured within a few days after sample preparation for synchrotron measurements (1st experiment). As can be seen in Fig. S1, the Laue fringes are clearly seen around (002) Bragg reflection of Ca_3SnO for the "1st experiment". From the observed Laue fringes pattern, we have estimated the thickness of Ca_3SnO layer to be about 13 nm. Since the total deposition time was about 3000 seconds, the deposition rate could be calculated to be ~0.004 nm/sec.

However, it should be noted that some chemical reaction may occur in the interface region of Ca_3SnO during Au deposition process as well as the XRD measurements in air. In fact, the intensity corresponding the "impurity phases" significantly depended on samples of Au/Ca_3SnO, which might originate from the difference in Au deposition conditions and from the elapsed time between sample fabrication and XRD measurements. Furthermore, as can be seen in Fig. S1, the chemical reaction continuously progresses even though the surface is protected by Au layer and the sample is stored in the vacuum desiccator (~10^{-1} Torr). The progressive reaction at the interface region is confirmed by an increment of the intensity of impurity phases after couples of months (2nd experiment: a black line) from the 1st experiment. Simultaneously, the Laue fringes around Ca_3SnO (002) Bragg reflection in the 1st experiment became unclear (but

still there) in the 2nd experiment. These results suggest that the chemical reaction at the interface occurs during the Au deposition process and progresses even after Au layer capping. Thus, the estimated film thickness (deposition rate) is underestimated in the present case.

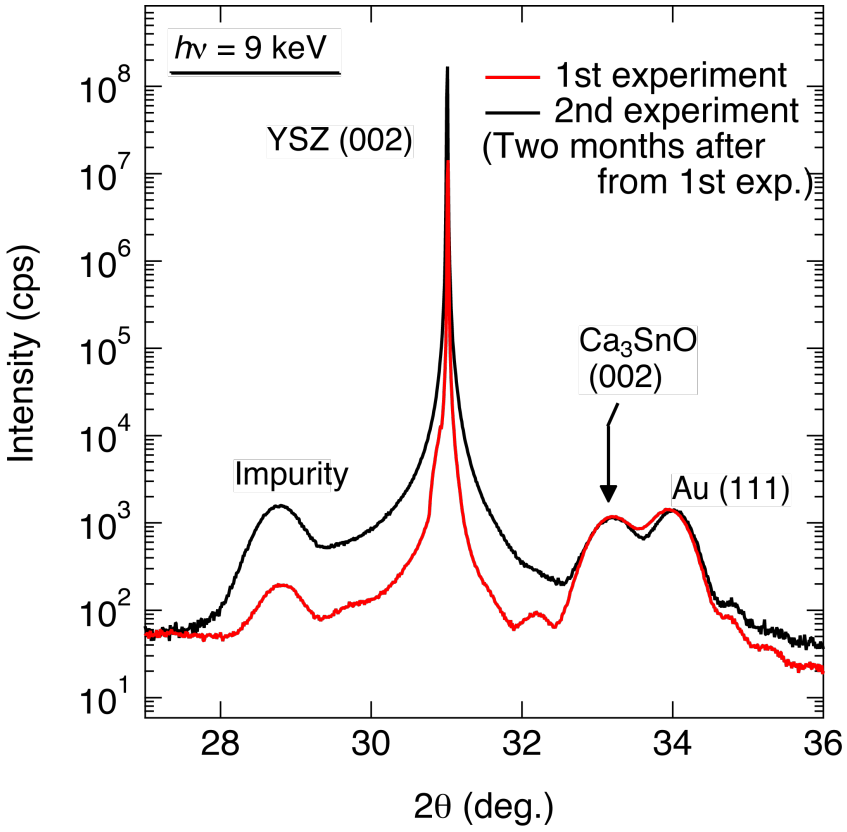

Fig. S1. Synchrotron-radiation based XRD patterns which are magnified around the (002) diffraction of Ca_3SnO film. A red line is identical to the 2θ-θ XRD pattern shown Fig. 1(a), which is measured within a few days after sample preparation for synchrotron measurements (1st experiment). Clear Laue fringes are observed around (002) Bragg reflection of Ca_3SnO. From the observed Laue fringes pattern, we have estimated the thickness of Ca_3SnO layer to be about 13 nm. The fringes pattern become unclear after two months (2nd experiment) from the 1st experiment, suggesting that the chemical reaction at the interface of Ca_3SnO progress even after Au layer capping.

Out-of-plane and in-plane lattice constants of Ca_3SnO film

Figure S2 shows the reciprocal space map (RSM) around (204) Bragg reflections of the Ca_3SnO film and the YSZ substrate. From the RSM results, the in-plane and out-of-plane lattice constants are estimated to be 0.481 ± 0.001 and 0.480 ± 0.001 nm, respectively. The almost identical values of both the lattice constant indicate that the Ca_3SnO film is fully relaxed owing to a large mismatch of 7.1 % between a Ca_3SnO film and a YSZ substrate [S2]. The slight deviation from the bulk value of 0.483 nm [S1] suggest the possible off-stoichiometry in the film.

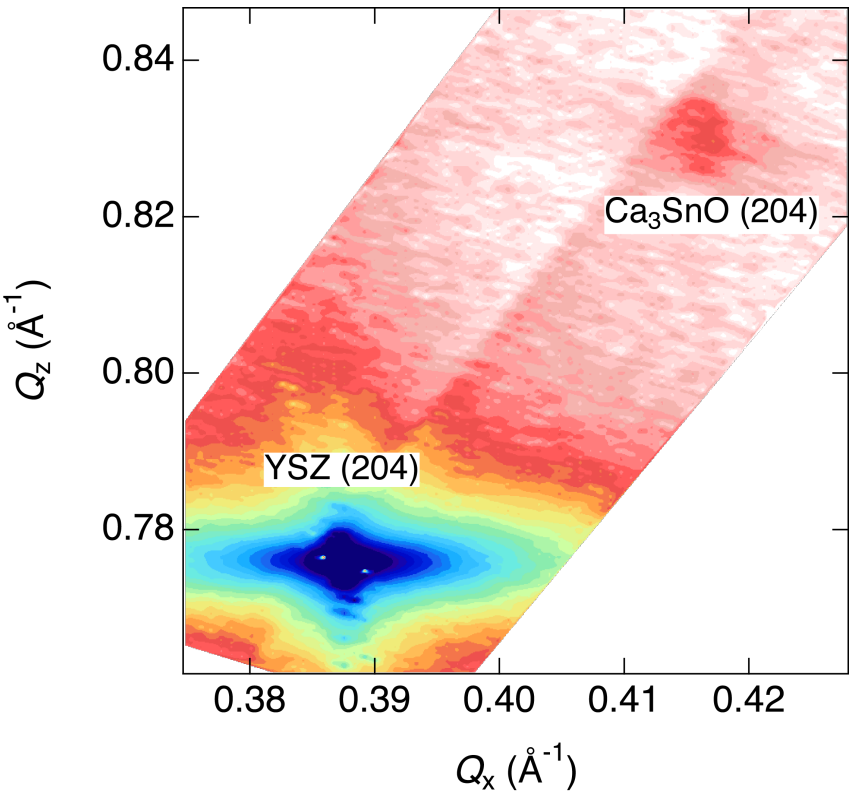

Fig. S2. Reciprocal space map around (204) Bragg reflections of a Ca_3SnO film and a YSZ substrate.

Growth-condition dependence of XRD pattern of Ca_3SnO films

Figure S3 shows the growth condition dependence in XRD and RHEED patterns of Ca_3SnO films. Since all samples that were characterized by RHEED in the Fig. 1 of the text were not protected by Au-capping layer and hence completely degraded, we have made the samples again with almost the same conditions. Here, we used Pt as a capping layer instead of Au, since Au (111) peak partially hinder the Ca_3SnO (002) peak. It should be noted that the Pt with the thickness of ~20 nm was deposited inside the PLD chamber just after the Ca_3SnO film growth in order to minimize the chemical reaction occurring at the interface between the capping layer and Ca_3SnO film. Furthermore, the XRD measurements have been performed within a couple of days after sample growth.

In RHEED patterns in Fig. S3(b), the chemical trend is almost identical to that of previous ones [Fig. 1(a)], indicating the high reproducibility of the present Ca_3SnO growth. In the case of optimum growth conditions (P_{O2} = 10^{-6}–10^{-7} Torr at $T_{sub.}$ = 700–750 ºC), the intensity of the "impurity" peaks in XRD pattern is negligibly weak as shown in Fig. S3(a). This result indicates that the intensity of the "impurity" signal in XRD pattern in Fig. 2(a) originates from the chemical reaction at the interface between Au and Ca_3SnO. Meanwhile, the intensity of impurity peak around the 2θ = 32º becomes prominent outside of optimum growth conditions. Notably, at the higher temperature of $T_{sub.}$ = 830 °C (α phase corresponding to a CaO film) only "impurity" peak is observed, and Ca_3SnO (002) peak disappears. Since Sn vanishes from the film at this temperature as shown in Fig. 1(b), we can assign this impurity peak as the CaO (111) from the peak position [see Fig. 2(b)].

The substrate-temperature ($T_{sub.}$) and oxygen-partial-pressure (P_{O2}) dependence of out-of-plane lattice constants are also summarized in Fig. S3(c). The lattice constant seems to not depend on $T_{sub.}$, while it slightly increases with increasing the P_{O2}.

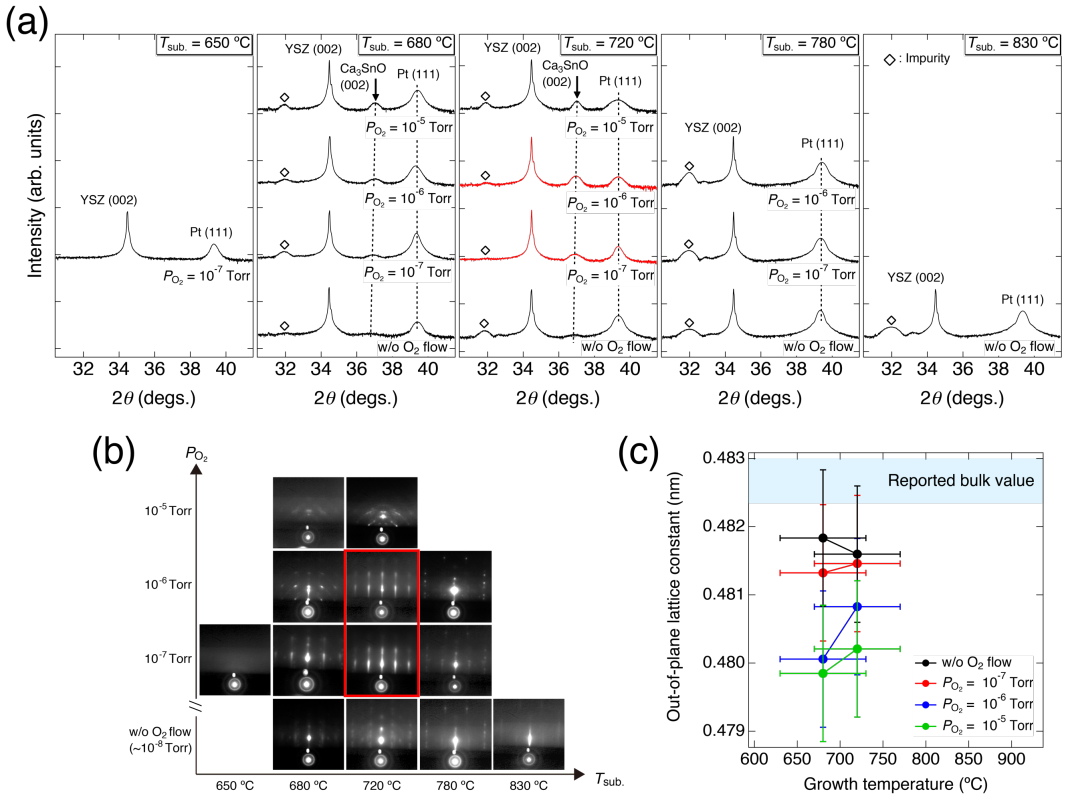

Fig. S3. (a) A map of XRD patterns of Ca_3SnO thin films grown on a YSZ (001) substrate at various $T_{sub.}$ and P_{O2}. The diamonds indicate the peaks from "impurities". XRD patterns for the optimum conditions (P_{O2} = 10^{-6} –10^{-7} Torr at $T_{sub.}$ = 720 ºC) are highlighted as red lines. (b) Corresponding RHEED patterns, where the optimum conditions are highlighted as red boxes. (c) The plot of out-of-plane lattice constants for the grown Ca_3SnO films as a function of $T_{sub.}$ and P_{O2}. The highlighted region corresponds to the reported bulk value of Ca_3SnO [S1].

Angular dependence of XPS spectra for a Sn-3*d* core level

Figure S4 shows angular dependent XPS spectra from the Ca_3SnO film for a Sn-3*d* core level. Since the intensity of the peaks at higher (lower) binding energies becomes stronger (weaker) with increasing photoelectron emission angle θ, the higher (lower) peaks are assigned to the surface (bulk) components.

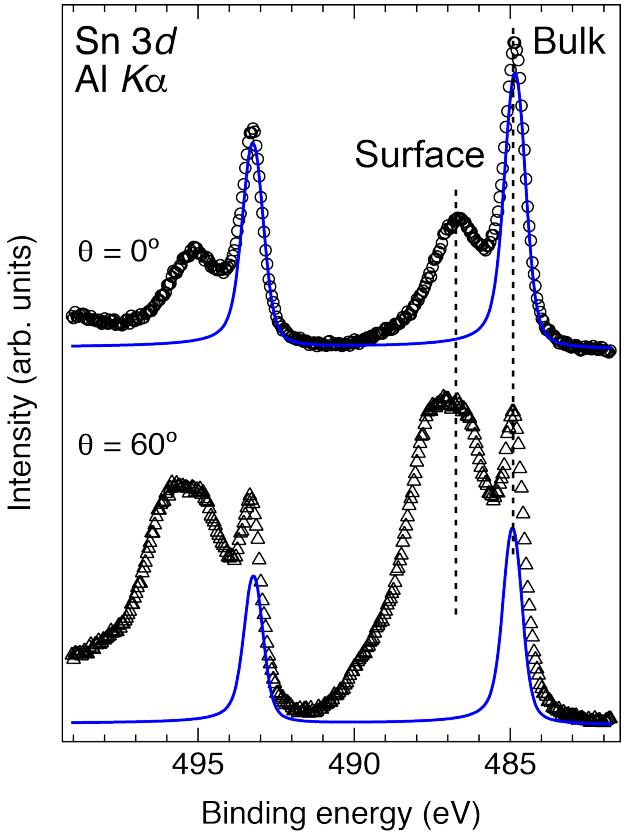

Fig. S4. Angular (surface-sensitivity) dependent XPS spectra from the Ca_3SnO film for a Sn-3*d* core level. Note that the sample is the same as the sample β in the main text. The fitted bulk components are overlaid by blue curves.

References

[S1] A. Widera and H. Schäfer, Mater. Res. Bull. **15**, 1805 (1980).

[S2] I. R. Gibson, and T. S. Irvine, J. Mater. Chem. **6**, 896 (1996).